Development and Integration of Flight Dynamics Models for Study of eVTOL Aircraft in the NASA Vertical Motion Simulator

David Caudle **Raghuvir Singh** **Carlos Malpica**
Aerospace Engineer
Aeromechanics Branch
NASA Ames Research Center
Moffett Field, CA, USA

Samuel J. Nadell **Tom Berger**
U.S. Army Combat Capabilities
Development Command
Aviation & Missile Center
Moffett Field, CA, USA

Peter Suh
Aerospace Engineer
Flight Dynamics and Controls Branch
NASA Armstrong Flight Research Center
Edwards, CA, USA

ABSTRACT

A piloted simulation study in the Vertical Motion Simulator at NASA Ames Research Center will investigate the handling and ride qualities of eVTOL configurations (lift-plus-cruise and tiltwing) for both civilian and military applications. The flight dynamics models were developed in the FLIGHTLAB modeling and analysis software environment, while explicit model-following control laws and high-fidelity powertrain models were developed in Simulink. The Joint Input-Output method was used to generate frequency responses for linear model verification, as the control effectors are highly correlated for these types of vehicles. The linear models were verified for the frequency range of interest for handling qualities. Once verified and tested individially, the three parts (flight dynamics model, control laws, and powertrain) will be integrated into the Vertical Motion Simulator for piloted simulation evaluations.

NOTATION

Symbols

C_g	Bus capacitance
I	Current (A)
$I_{xx}, I_{yy}, I_{zz}, I_{xz}$	Products of Inertia
L, M, N	Vehicle angular moments
L_p, M_q	Dimensional damping derivatives
M_u, L_v, M_w	Dimensional speed stability derivatives
L_Q, L_Ω	Roll Derivatives for rotor torque and speed
N_Q, N_Ω	Yaw Derivatives for rotor torque and speed
p, q, r	Body axis rates (rad/s)
P_g	Generator power
Q_r	Rotor torque (ft-lb)
r	Reference input for JIO method
u, v, w	Body velocities in the x, y, z directions (ft/s)
$\boldsymbol{u}$	Bare-airframe input vector
V	Voltage (V)
v	Virtual control effector input
$v_{i,wing}$	Induced velocity on the wing (ft/s)
$\boldsymbol{x}$	State vector
$\boldsymbol{y}$	Output vector
δ_A	Real control effector input
η	efficiency factor
ϕ, θ, ψ	Vehicle attitudes (rad)
τ_g^c	Generator torque command (ft-lb)
Ω	Rotor speed (rad/s)
ω_g^r	Generator rated speed (RPM)

Acronyms

EMF	Explicit Model-Following
ESC	Electronic Speed Controller
eVTOL	Electric Vertical Takeoff and Landing
HQTE	Handling Qualities Task Element
JIO	Joint Input-Output
MTE	Mission Task Element
NDARC	NASA Design and Analysis of Rotorcraft
(N)FW	(No) Flux Weakening
PID	Proportional-Integral-Derivative (control)
PMSM	Permanent magnet synchronous motor
RTPM	Real-Time Powertrain Model

Presented at the Vertical Flight Society's 81st Annual Forum & Technology Display, Virginia Beach, VA, USA, May 20–22, 2025.

SCAS	Stability & Control Augmentation System
UAM	Urban Air Mobility
VMS	Vertical Motion Simulator
VVPM	Viscous Vortex Particle Method

INTRODUCTION

The growing number of electric vertical takeoff and landing (eVTOL) vehicles has prompted many research efforts to better understand the usefulness and limitations of these vehicles. At the beginning of 2025, there were over 1,000 concepts from 400+ designers (Ref. 1). A large emphasis has been placed on Urban Air Mobility (UAM) operations, however many use cases for these vehicles are being studied for both military and civilian applications including disaster relief, firefighting, medical evacuation, and personnel movement (Ref. 2). While there are some unique outlier designs, many aircraft designers have converged on several common configurations that can be generally classified as (1) vectored thrust, (2) wingless/multicopter, and (3) lift-plus-cruise. Much research already exists for multicopter rotorcraft, particularly quadrotors, but less so for vectored thrust and lift-plus-cruise vehicles. A research effort in the NASA Ames Vertical Motion Simulator (VMS) is planned to evaluate the handling qualities of these types of vehicles, with a particular focus on the transition from low to high speed flight.

Recent handling qualities (HQ) experimental work from Refs. 3–5 centered primarily on the evaluation of heave, attitude, and translational rate response characteristics of UAM RPM-controlled eVTOL in hover and low speed. Initial versions of the electrified powertrain models used here were tested in Refs. 3, 6, and 7, demonstrating the potential for significant handling qualities degradation (including full loss of control) associated with the control-authority limitations caused by the activation of powertrain limits of tightly integrated propulsion and flight control systems.

A key premise of Refs. 3–7 is that agility demands for UAM operations differ significantly from military use cases. Hence, while offering useful design guidelines for civilian applications, established military handling qualities specifications may be overly conservative. Accordingly, basic handling qualities sensitivities to varying aggressiveness and precision performance requirements were investigated.

This assumption is also reflected by the major regulatory agencies. Furthermore, the FAA and EASA/EUROCAE have been studying the potential of HQ flight testing as one of the tools for certification (Refs. 8–10). The proposed approach envisions the use of flight test maneuvers akin to the Mission Task Element (MTE) maneuvers from ADS-33 for applicants to demonstrate the safety of their aircraft. Compared to ADS-33 MTEs, Handling Qualities Task Element (HQTE) maneuvers proposed in Ref. 8 present relaxed aggressiveness performance requirements. These publicly available draft HQTEs now present a reference to guide the foundational research that can inform future handling qualities predictive metrics or standards for UAM.

The proposed research supported by the models being discussed will continue to explore the HQ, for both UAM and military operations, of these new types of aircraft from hover to forward flight and transition between the two. A few points of emphasis for experimentation will be to: (1) collect data to substantiate the formulation of predictive HQ design standards for UAM, based on draft HQTE maneuvers in the public domain; (2) further vet HQTE maneuvers for their ability to expose objectionable characteristics of highly augmented eVTOL; (3) examine suitability of eVTOL for potential military applications; and (4) assess the cabin vibrations for acceptable passenger ride qualities.

AIRCRAFT MODELS

The flight dynamics models were initially developed in FLIGHTLAB by Advanced Rotorcraft Technology, Inc. (Ref. 11), derived from the lift-plus-cruise and tiltwing NASA reference vehicle models (Refs. 12,13). Table 1 highlights basic characteristics of each vehicle while further details will be described later in this section. Trim, linearization, and frequency sweeps of the bare airframe were performed in FLIGHTLAB while system identification was performed in

Table 1. Characteristics of Lift-Plus-Cruise and Tiltwing Models

Characteristic	Lift-Plus-Cruise	Tiltwing
Operating Weight	6650 lb (3016 kg)	6595 lb (2991 kg)
Capacity	6 people	6 people
Wingspan	47.7 ft (14.5 m)	43.7 ft (13.3 m)
Length	32 ft (9.74 m)	28 ft (8.5 m)
Cruise Speed	122 kt	145 kt
Number of Rotors	8 lifting, 1 pusher	6 main, 2 tail
Blades Per Rotor	2 (lifting), 6 (pusher)	5
Rotor Radius	5 ft (1.52 m), 4.5 ft (1.37 m)	3.64 ft (1.11 m)

CIFER. A full flight envelope controller was developed for each aircraft. The controllers were developed in Simulink and optimized using CONDUIT.

Lift-Plus-Cruise Concept Vehicle

The lift-plus-cruise vehicle enables helicopter-like flight at hover and low-speed and, similar to a fixed-wing aircraft, performs fully wing-borne flight at higher speeds, where it is intended to spend most of its flight time. The vehicle has eight lifting rotors with fixed pitch and variable speed. The rotors are modeled as stiff, two-bladed rotors. The inboard rotors are canted outward eight degrees to reduce risk of passenger injury in case of catastrophic rotor failure. Additional design rationale can be found in Ref. 12. At hover and low speeds, all or most of the lift is produced by the rotors. As the vehicle increases airspeed, the lifting rotors reduce speed, decreasing their lift contribution as the wing becomes more effective. At 85 kts, the lifting rotors are stopped and locked in a minimum drag position, aligned with the pylons. At this point, the vehicle flies like a fixed-wing aircraft with traditional control surfaces. A pusher propeller of constant speed and variable pitch on the tail of the aircraft controls forward airspeed in all flight regimes. A top-down view of the vehicle with numbered rotors in the cruise configuration is shown in figure 1.

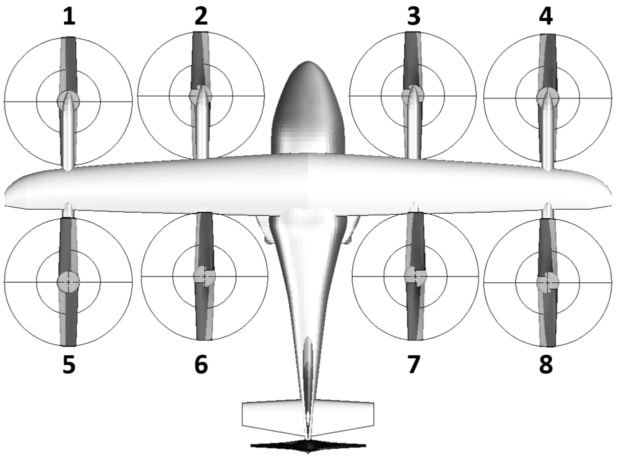

Figure 1. Top view of lift-plus-cruise model with numbered rotors.

Rotors are blade element models with stiff flap dynamics and airloads determined from lift, drag, and moment coefficients as functions of angle of attack, Mach number, and dynamic pressure. The Viscous Vortex Particle Method (VVPM) was used to calculate the self-induced inflow effects as well as rotor-on-rotor interference (Ref. 11), while a Peters-He dynamic inflow model is used for real-time simulation. In the cruise configuration, airloads for the stopped rotors were based on CFD lookup tables.

The FLIGHTLAB model transitions from rotor-borne to fully wing-borne at 85 kts. While this has no effect on static analyses, simulating flight through this region could become problematic if the aircraft dwells at 85 kts and the rotors are turning on and off rapidly. To allow for a smoother transition and prevent simulation instabilities around this airspeed, a transition hysteresis was developed to expand the transition region and better ramp up or down the rotors. The aircraft was trimmed in level flight with rotors on up to 100 kts and then again with rotors off down to 75 kts. Figure 2 shows the trimmed pitch attitude with rotors on and rotors off with overlap occurring in the transition region. With rotors off, the angle of attack, and therefore pitch attitude, required to trim increased significantly as airspeed decreased. In the model-following control laws, the rotor transition was expanded to stop rotors at 95 kts when accelerating and start them again at 85 kts when decelerating, eliminating the single speed transition point.

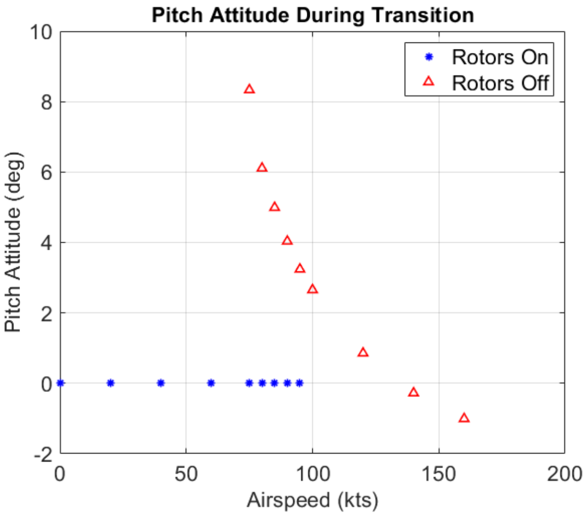

Figure 2. Lift-plus-cruise transition flight comparison with rotors on and off.

Lift-Plus-Cruise Cabin Vibrations

Cabin vibrations of high amplitude or at specific frequencies may result in passenger discomfort. While the real-time model uses a rigid body fuselage, an elastic fuselage was modeled to look at how the vibratory hub loads cause cabin vibrations. As the lift-plus-cruise vehicle increases in airspeed in rotor-borne flight, the vibrations increase as well, peaking near the transition speed of 85 kts. An early investigation into expected vibration levels was performed at 80 kts, just prior to rotors shutting off (at which point hub vibrations cease). Both rigid and elastic airframes were used to compare vertical accelerations experienced in the cabin. The elastic airframe included the modal properties of the wing, fuselage, all 8 lifting rotors, and pusher propeller. To elicit a vibration response, a 50 ft-lb torque doublet was applied to all rotors. Input amplitude was selected to produce enough of an aircraft response while maintaining the flight condition throughout the maneuver. The input was applied 10 seconds into the run so that a steady-state vibration baseline could be established. Peak accelerations occurred during the doublet input, shown in Fig. 3.

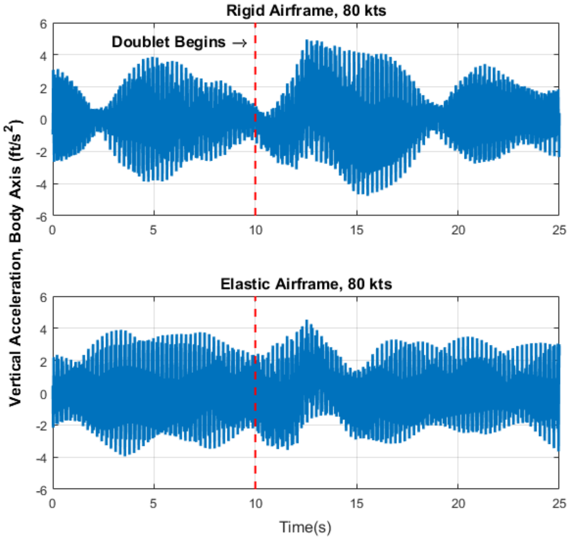

Figure 3. Vertical acceleration of rigid and elastic airframes due to rotor collective doublet input.

The beating effect observed is most notable in the rigid airframe, but present in both rigid and elastic airframes and is due to the front and rear rotors spinning at slightly different speeds for level flight. A max peak-to-peak acceleration of 8.7 ft/s^2 (0.27 g) at 13-15 Hz for the rigid airframe and a max peak-to-peak acceleration of 7.8 ft/s^2 (0.24 g) at 15-17 Hz for the elastic airframe was observed. Techniques for classifying the effect on the human body at these vibration frequency and magnitudes as discussed in Ref. 14 will be used for further vibration analysis.

Tiltwing Concept Vehicle

Tiltwing aircraft are compelling vehicles to investigate for the UAM mission due to the potential for increased airspeed and reduced noise when compared to conventional rotorcraft or even some unconventional designs such as the lift-plus-cruise. The tiltwing does not cruise with rotors in edgewise flight, allowing the vehicle to have a higher cruise speed and typically reduced noise (Ref. 13). The tiltwing also benefits from using shared lift/thrust effectors, as the rotors do not need to be stopped, which reduces weight and drag penalties. The tiltwing developed for this study, shown in Fig. 4, has eight total rotors – six along the main wing and two on the horizontal T-tail. The entire main wing and tail rotors rotate 90 degrees, pointing upward at hover. They tilt forward at the same rate and are scheduled with airspeed until they are fully horizontal at 110 kts. For this study, a link was maintained between the wing tilt angle and tail rotor tilt angle. For the remainder of this paper, all mentions of wing tilt angle implicitly indicate tail rotor tilt angle as well.

The rotors are modeled as stiff (no flap or lead-lag dynamics), five-bladed, and collective-controlled. Rotor tip speed is 550 ft/s for low speed and transition flight. Once the wing is tilted forward, the rotor tip speed decreases to 300 ft/s for wing-borne flight. Interference effects of the main rotors on the main wing and tail rotors were calculated with VVPM. Yaw control of this vehicle at hover is controlled by aileron deflection as rotor wash flows over the wing.

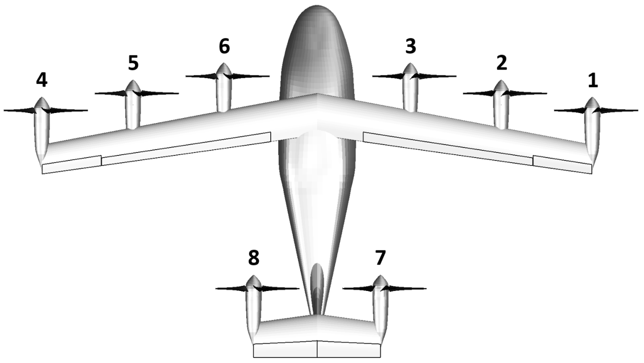

Figure 4. Top view of tiltwing model with numbered rotors.

The tiltwing configuration does not have a well defined transition region like the lift-plus-cruise. The wing and tail rotors are scheduled to tilt across the majority of the flight envelope (5-110 kts) compared to the 10 kt transition range for the lift-plus-cruise. Since many different combinations of pitch attitude and wing-tilt angles can produce a trimmed condition at a given airspeed, the ideal wing-tilt angle for a given airspeed was investigated. Ideal wing-tilt angle was defined as the angle for which vehicle pitch attitude was zero, as this was assumed to be ideal for passenger comfort. Trim conditions were calculated from hover up to 140 kts in 10 kt increments. Zero degree pitch attitude was held constant and the wing-tilt angle was used as a trim variable while flaps were scheduled with airspeed. Once the ideal transition curve was established, the wing-tilt angle was offset by ±3, 6, and 9 degrees and held fixed while the pitch attitude was used as a trim control. This allowed an initial transition corridor to be established. The ideal tilt angles were used as trim and linearization points, but the expanded corridor is shown in Fig. 5. The blue regions

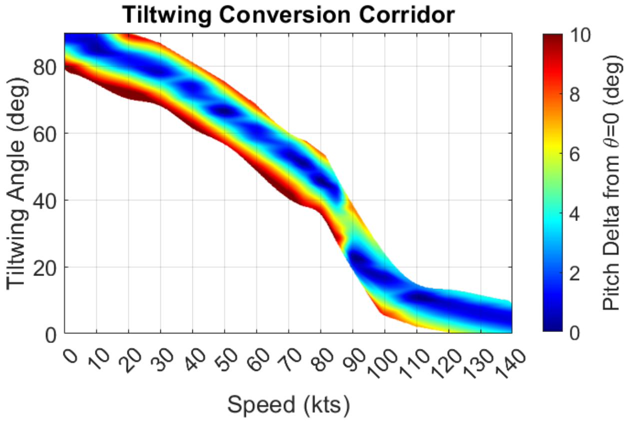

Figure 5. Tiltwing conversion corridor for level flight.

along the center of the corridor indicate low pitch attitudes required to trim while the yellow and red regions, primarily at lower airspeeds and wing tilt angles, are higher pitch attitudes required. In the abscense of clear passenger comfort guidance, the trim pitch attitude was limited to ±10 degrees. Note that between 85 and 90 kts, the vehicle was unable to trim with zero pitch attitude in its current configuration. Additional details for both models can be found in Refs. 11 and 15.

MODEL LINEARIZATION AND VERIFICATION

Linear Models

Linear models were required to develop the explicit model-following (EMF) controller. Linearization was performed within FLIGHTLAB, which perturbs each state and control from a trimmed condition. The change in the forces, moments, and outputs for each perturbation is stored for each time step and then averaged over one rotor revolution to obtain the state, control, and output matrices.

The lift-plus-cruise and tiltwing models were reduced to 17 and 12 states, respectively. Each model included the nine rigid body states plus eight rotor speed states for the lift-plus-cruise and three wing induced velocity states for the tiltwing. The wing induced velocity states are most important at hover as flow over the wing is used to control yaw. The inputs to the linear model were considered to be the bare-airframe inputs for each vehicle. The lift-plus-cruise state and input vectors are shown in Eq. 1, while the tiltwing state and input vectors are shown in Eq. 2.

$$\boldsymbol{x}_{\text{lpc}} = \begin{bmatrix} \phi \\ \theta \\ \psi \\ p \\ q \\ r \\ u \\ v \\ w \\ \Omega_{1-8} \end{bmatrix}, \quad \boldsymbol{u}_{\text{lpc}} = \begin{bmatrix} Q_{r1} \\ Q_{r2} \\ Q_{r3} \\ Q_{r4} \\ Q_{r5} \\ Q_{r6} \\ Q_{r7} \\ Q_{r8} \\ \delta_{\text{ail}_\text{L}} \\ \delta_{\text{ail}_\text{R}} \\ \delta_{\text{elev}} \\ \delta_{\text{rud}} \\ \theta_{r9} \end{bmatrix}, \tag{1}$$

$$\boldsymbol{x}_{\text{tiltwing}} = \begin{bmatrix} \phi \\ \theta \\ \psi \\ p \\ q \\ r \\ u \\ v \\ w \\ v_{i,\text{wing},1-3} \end{bmatrix}, \quad \boldsymbol{u}_{\text{tiltwing}} = \begin{bmatrix} \theta_{r1} \\ \theta_{r2} \\ \theta_{r3} \\ \theta_{r4} \\ \theta_{r5} \\ \theta_{r6} \\ \theta_{r7} \\ \theta_{r8} \\ \delta_{\text{ail}_\text{L}} \\ \delta_{\text{ail}_\text{R}} \\ \delta_{\text{elev}} \\ \delta_{\text{rud}} \end{bmatrix} \tag{2}$$

The linear models were obtained at sea level for airspeeds 0, 40, 80, and 120 knots in a nominal c.g. configuration. Speeds were selected based on past work indicating that stability derivatives change gradually as airspeed increases (Ref. 16). A look at the rigid body stability derivatives in Fig. 6 indicate the lift-plus-cruise configuration follows this trend as well. In both figures, the blue stars represent the rotors on cases while the red triangles represent rotors off. The damping derivatives (L_p and M_q) both begin as small negative values in hover and linearly decrease as airspeed increases. The M_u and L_v derivatives remain relatively constant and near zero throughout the entire flight envelope, typical of fixed-wing aircraft. M_w is approximately zero from hover to 40 kts and then it begins to go more negative as speed increases, continuing this trend in wing-borne flight. For all derivatives, the transition region overlaps closely among rotors on/off. Trim points used for control law development are indicated with black squares.

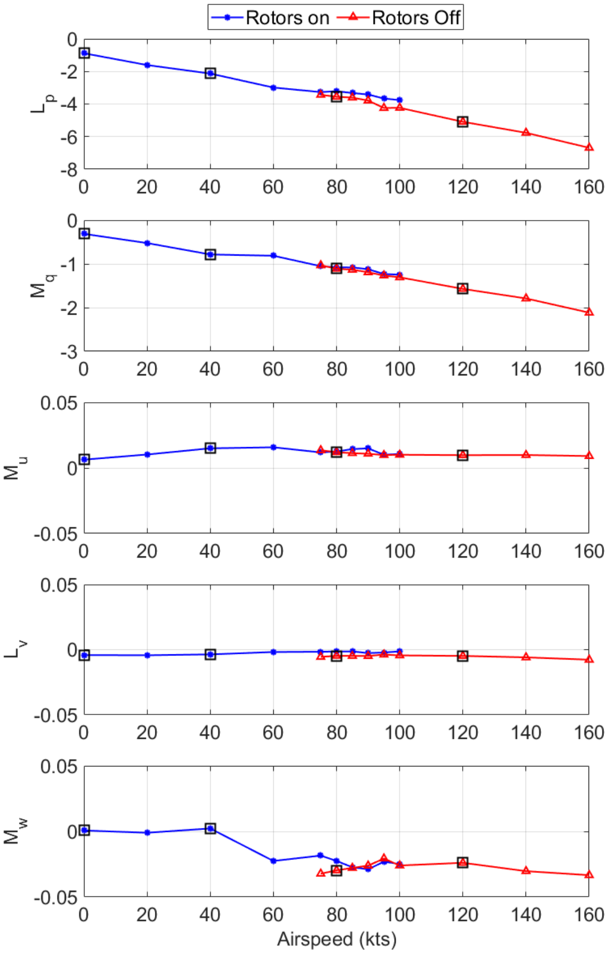

Figure 6. Lift-plus-cruise damping and speed stability derivative trends for rotors on and off from 0-160 kts.

The gradual change in stability derivatives is true for the tiltwing damping derivatives as well (Fig. 7). The roll damping (L_p) remains constant near zero until 80 kts, at which point it begins to decrease linearly. The pitch damping (M_q) follows a negative, linear trend, increasing in magnitude as airspeed increases, similar to the lift-plus-cruise. The speed stability derivative (M_u) begins positive, near zero, slightly decreasing through 80 kts. From 80 to 120 kts, variations in M_u occur as the vehicle transitions from primarily rotor-borne to primarily wing-borne flight. These variations can be reduced by tuning the wing flap angle for these flight conditions, however for this paper the flap deflection was solely a function of airspeed. L_v remains near zero throughout the flight envelope, with a slight increase in that same transition region around 100 kts. M_w decreases linearly at low speed until the main transition region and then increases, leveling off just below zero at high speed.

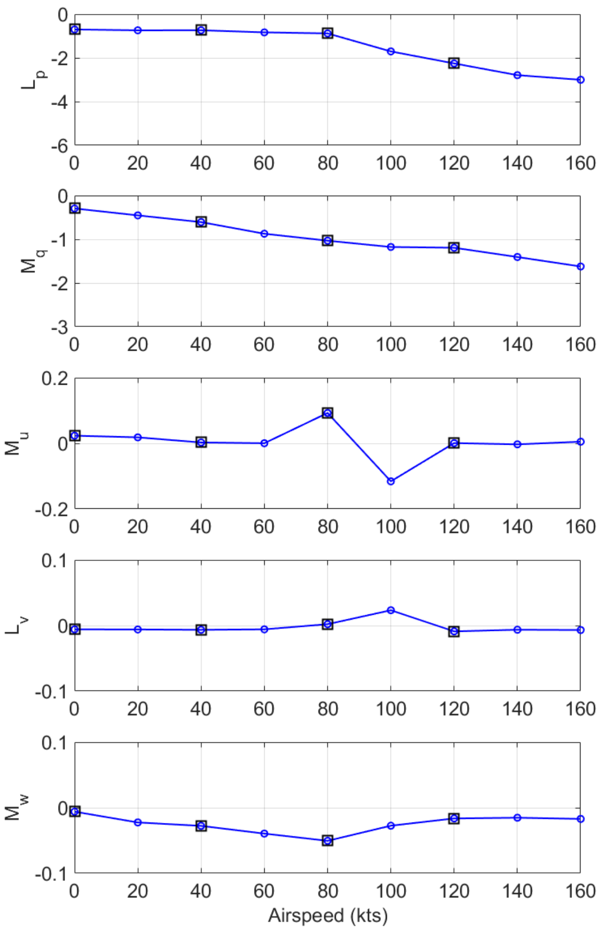

Figure 7. Tiltwing damping and speed stability derivative trends from 0-160 kts.

Linearization Verification

Verification of the linear models extracted from FLIGHTLAB using small perturbations was conducted to ensure the linear models accurately represented the dynamics of the nonlinear model. Verification was done by performing time-domain frequency sweeps of the nonlinear FLIGHTLAB model, identifying frequency responses from the time-domain data, and comparing the identified frequency responses with those of the linear models. Verification was performed for all input-output pairs.

Typically, to identify frequency responses for multi-input/multi-output systems, each input is excited one at a time using a frequency sweep signal, the inputs and outputs are measured, and input-output cross spectral density function and input auto spectral density functions are extracted from the windowed time history data and used to identify individual frequency responses. This method is referred to as the Direct Method for system identification and can be used when the inputs are at most partially correlated (Ref. 16).

For the lift-plus-cruise and tiltwing models, which are bare-airframe unstable in hover, frequency sweeps must be performed with a controller engaged. Furthermore, because both aircraft are over-actuated (more inputs than degrees of freedom being controlled), a mixer (or control allocation) matrix is included in the controller, which distributes the control system command to all of the individual bare-airframe effectors. A notional block diagram of the bare-airframe $\boldsymbol{P}$, controller $\boldsymbol{C}$, and FLIGHTLAB mixing matrix $\boldsymbol{M}_{FLAB}$ is shown in Fig. 8. This results in highly correlated bare-airframe inputs during frequency sweeps, which means the Direct Method for frequency response identification cannot be applied.

For the frequency response identification used for linearization verification, the Joint Input-Output (JIO) method (Ref. 17), was applied. In the JIO Method, both the inputs and outputs of the bare-airframe are considered jointly as outputs to a set of uncorrelated reference inputs, r.

The reference inputs are defined to excite symmetric and differential groups of effectors (referred to as virtual effectors) to concentrate the vehicle response to a primary axis, which results in higher signal-to-noise ratio and coherence during identification (Refs. 17, 18). The reference inputs are related to the individual bare-airframe effectors (Eqs. 1 and 2) by the mixing matrix, $\boldsymbol{M}$. The reference inputs for the lift-plus-cruise and tiltwing configurations are shown in Eq. 3.

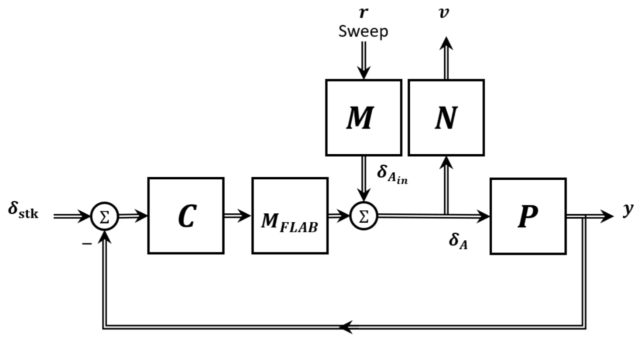

Figure 8. Block diagram showing the locations of the reference input frequency sweeps and other key signals for model validation.

$$r_{\text{lpc}} = \begin{bmatrix} \text{outer}_{\text{lat}} \\ \text{outer}_{\text{long}} \\ \text{outer}_{\text{heave}} \\ \text{outer}_{\text{dir}} \\ \text{inner}_{\text{lat}} \\ \text{inner}_{\text{long}} \\ \text{inner}_{\text{heave}} \\ \text{inner}_{\text{dir}} \\ \text{ail}_{\text{sym}} \\ \text{ail}_{\text{diff}} \\ \delta_{\text{elev}} \\ \delta_{\text{rud}} \\ \theta_{r9} \end{bmatrix}, \qquad r_{\text{tiltwing}} = \begin{bmatrix} \text{outer}_{\text{sym}} \\ \text{outer}_{\text{diff}} \\ \text{mid}_{\text{sim}} \\ \text{mid}_{\text{diff}} \\ \text{inner}_{\text{sym}} \\ \text{inner}_{\text{diff}} \\ \text{tail}_{\text{sym}} \\ \text{tail}_{\text{diff}} \\ \text{ail}_{\text{sym}} \\ \text{ail}_{\text{diff}} \\ \delta_{\text{elev}} \\ \delta_{\text{rud}} \end{bmatrix} \tag{3}$$

Grouping, or ganging, the individual bare-airframe effectors with the matrix $\boldsymbol{N} = \boldsymbol{M}^{-1}$ produces the virtual effectors, $\boldsymbol{v}$, which are then used to identify the system. Frequency responses of the aircraft to the virtual effectors ($\boldsymbol{y}/\boldsymbol{v}$) were identified using the Direct method for cases with limited input correlation and the JIO methods for cases with high input correlation.

The lift-plus-cruise rotors were grouped into "outer" (rotors 1, 4, 5, and 8) and "inner" (rotors 2, 3, 6, and 7) rotor groups and excited symmetrically or differentially to achieve responses in the primary axes of control. The tiltwing rotors were split into four rotor groups: outer (1 and 4), middle (2 and 5), inner (3 and 6), and tail (7 and 8). An aileron group was also included to excite the yaw axis at hover. Tables 2 and 3 show the lift-plus-cruise and tiltwing JIO groupings at hover for each reference input and the input signs for each rotor in the group. Each cell in the tables represent a single reference input sweep. The effectors excited with the respective sign are indicated. All other effectors are undisturbed. For example, a pitch response for the lift-plus-cruise configuration was obtained by injecting a positive sine sweep into rotors 1 and 4 and injecting an equal but negative sine sweep into rotors 5 and 8, highlighted in Table 2. Ninety second sine sweeps from 0.5 rad/s to 30 rad/s were performed for each reference input and the results were processed through CIFER. Inputs were ±10% of either steady-state value (rotor speed) or max deflection (control surfaces). A simple stability augmentation system employing PID control was used to maintain the trim flight condition. In total, eight sweeps were required for the lift-plus-cruise and ten sweeps were required for the tiltwing at hover. Note that for the tiltwing, the same sweep profile was used to identify the pitch and heave responses from the outer, middle, and inner rotor groups.

Lift-Plus-Cruise Frequency Response

The eight lifting rotors act as the primary control effectors at hover and low speed. Figures 9 – 12 show the on-axis response due to outer rotor group perturbations in hover. Off-axis responses for these cases were minimal due to selection of reference inputs. The responses show good correlation between the nonlinear and linear models as well as high coherence throughout the frequency range of interest (1-10 rad/sec).

Table 2. JIO Method Input Profiles for Lift-Plus-Cruise System Identification at Hover

	Rotor	Pitch	Roll	Heave	Yaw
Outer	1	+	+	+	+
	4	+	-	+	-
	5	-	+	+	-
	8	-	-	+	+
Inner	2	+	+	+	+
	3	+	-	+	-
	6	-	+	+	-
	7	-	-	+	+

Table 3. JIO Method Input Profiles for Tiltwing System Identification at Hover

	Rotor/ Surface	Pitch	Roll	Heave	Yaw
Outer	1	+	-	+	
	4	+	+	+	
Middle	2	+	-	+	
	5	+	+	+	
Inner	3	+	-	+	
	6	+	+	+	
Tail	7	+	-		
	8	+	+		
Ailerons	L	+			-
	R	+			+

Once the aircraft exceeds 85 kts, the rotors are stopped and traditional control surfaces take over. Figures 13 through 15 show the roll, pitch, and yaw rate responses due to their respective control surfaces at 120 kts. Again, linear and nonlinear responses show very similar results. Frequency responses indicate the lift-plus-cruise configuration behaves like a conventional rotorcraft at hover and a conventional fixed-wing aircraft at high speed.

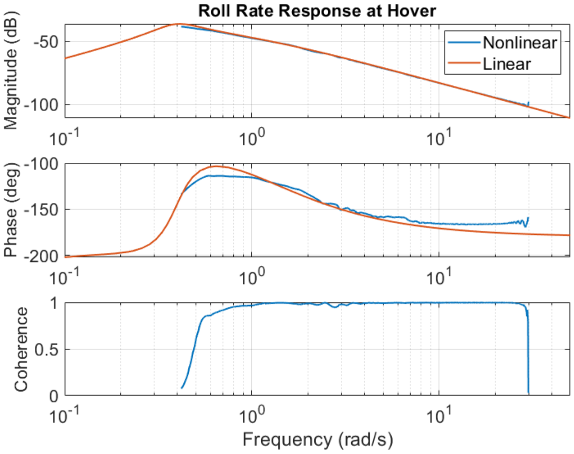

Figure 9. Lift-plus-cruise hover response for p/v_{roll}.

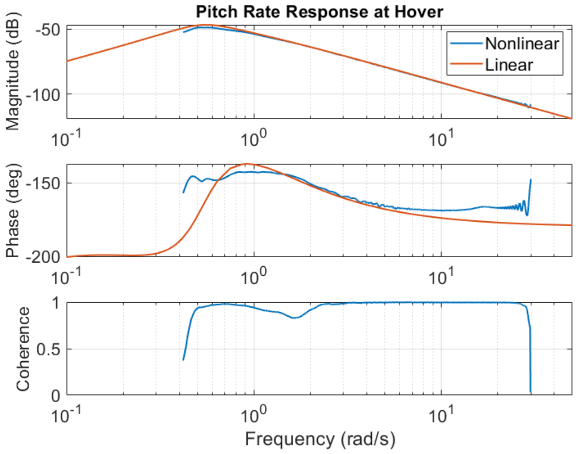

Figure 10. Lift-plus-cruise hover response for $q/v_{\mathbf{pitch}}$.

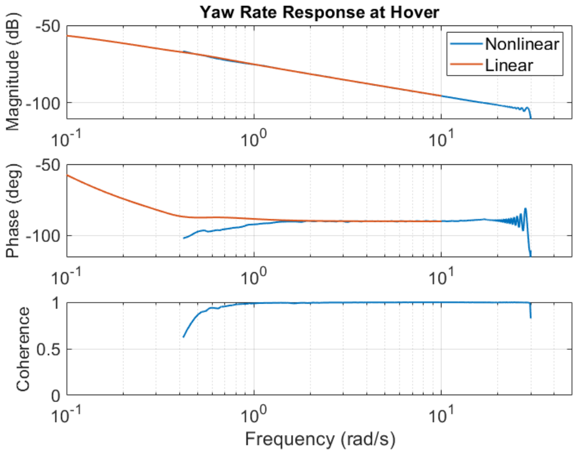

Figure 11. Lift-plus-cruise hover response for $r/v_{\mathbf{yaw}}$.

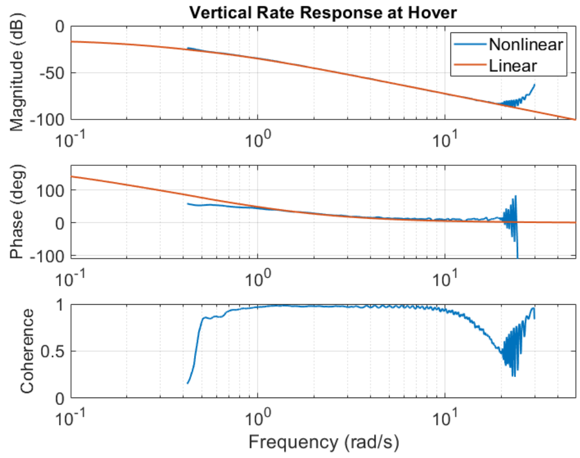

Figure 12. Lift-plus-cruise hover response for $w/v_{\mathbf{heave}}$.

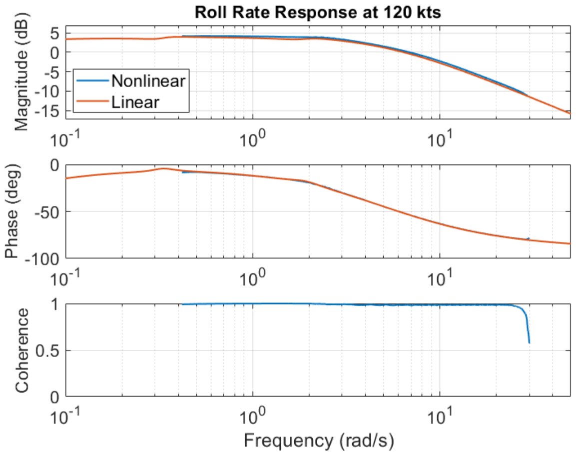

Figure 13. Lift-plus-cruise 120 kt response for $p/\delta_{\mathbf{ail}}$.

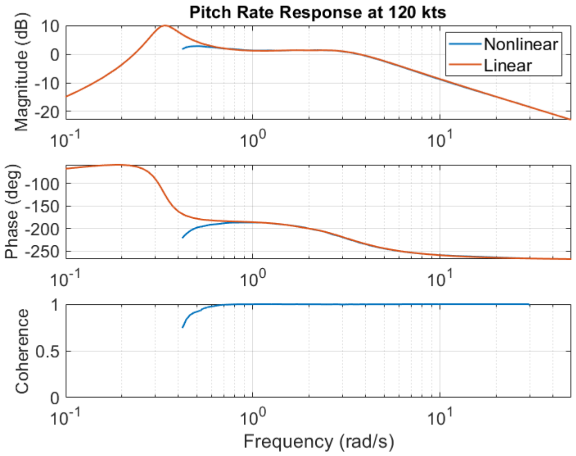

Figure 14. Lift-plus-cruise 120 kt response for $q/\delta_{\mathbf{elev}}$.

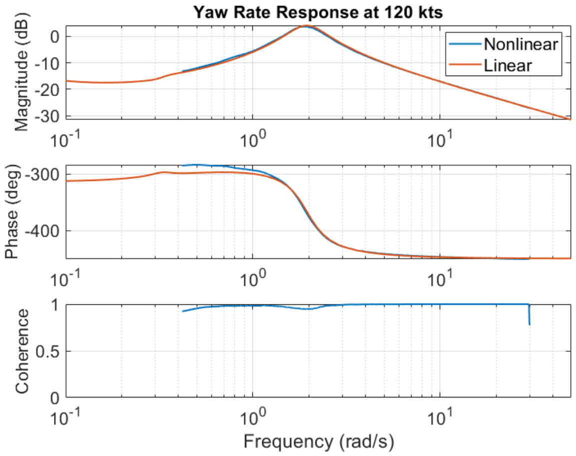

Figure 15. Lift-plus-cruise 120 kt response for $r/\delta_{\mathbf{rud}}$.

POWERTRAIN

Motor Simulation

The real-time powertrain modeling (RTPM) tool is used for development of powertrain models for VMS testing (Ref. 6). It was used to form the building blocks of the turboelectric lift-plus-cruise and tiltwing powertrain architecture. The RTPM sizing routine was also used to size motors for both concept vehicles (Ref. 19). It models the motor dynamics using a direct-quadrature model (Ref. 20) of a permanent magnet synchronous motor (PMSM). The RTPM tool takes in flight control law torque commands and outputs Q and D-axis voltages and currents for powertrain simulations.

The RTPM was tested in the VMS and found to be capable of running the turboelectric lift-plus-cruise powertrain simulation on a single computer thread at approximately 20 times faster than real-time. The paper detailing the development, verification, and validation of RTPM can be found in Ref. 7.

Power Sharing

For both the lift-plus-cruise and tiltwing vehicles, power sharing must be modeled. Power sharing among RTPM developed motors places a total power constraint on the vehicle control laws. The summed load from all motors drawing on peak power simultaneously may be too much for the generator power on the bus voltage leading to a precipitous drop of bus voltage to zero. A complete voltage loss may result in a complete loss of power for all motors connected to the voltage bus. An emergency battery is used for such an event, however it is a one-time-use battery so the generator was designed to never rely on the emergency battery for typical vehicle operations (Ref. 21).

The bus voltage of the turbogenerator for both the lift-plus-cruise and tiltwing is assumed to be governed by the dynamics of a capacitor as

$$C_b \dot{V}_{bus} = I \tag{4}$$

where C_b is the bus capacitance and I is the bus current. The bus current in Eq. 4 is computed as

$$I = \frac{\eta_I P_g}{V^g_{bus}} - \frac{P_l}{\eta_I \eta_c V_{bus}} \tag{5}$$

where P_g is the generator power, P_l is the load power, V^g_{bus} is the generator-side filtered bus voltage, V^l_{bus} is the load-side filtered bus voltage, η_I is the inverter efficiency, and η_c is a direct current (DC)-DC buck converter efficiency assumed to be 98%. A supercapacitor was assumed to be available on the voltage bus to reduce transients from high load power draws.

The generator motor power is computed as

$$P_g = \frac{3}{2}(V^g_q I^g_q + V^g_d I^g_d) \tag{6}$$

where the generator Q and D-axis voltages, V^g_q and V^g_d, and generator Q and D-axis currents, I^g_q and I^g_d, are computed by the RTPM tool. The load power is

$$P_l = \frac{3}{2}\sum_{i=1}^{N_m}(V^i_q I^i_q + V^i_d I^i_d) \tag{7}$$

where the index i refers to the ith motor for voltages and currents computed by the RTPM tool. For the turboelectric lift-plus-cruise simulation, there are 8 lifting motors and 1 pusher motor to be accounted for so the total number of motors, N_m, was equal to 9. For the tiltwing configuration, there are 6 main wing motors and 2 tail motors for a total of 8 motors.

The generator was assumed to operate at a fixed speed of 6,000 RPM, as specified by the NASA Design and Analysis of Rotorcraft (NDARC) tool. Commanded torque to the generator was assumed to be responsible for all generator power changes, because torque commands can more readily match power demand changes of the powertrain. When load power exceeds generator power, the generator torque is computed as a function of load power with the objective of reducing bus voltage transients. The torque command to the generator is

$$\tau^c_g \triangleq \frac{P_l}{\omega^r_g \eta_I} \tag{8}$$

where ω^r_g is the generator rated speed.

Motor Design

The lift-plus-cruise vehicle motor models were produced using the RTPM motor map development procedure. The source of key parameters used by RTPM, such as peak torque and maximum rated power, were provided by NDARC (Ref. 22). An example of the torque-speed map for the lift-plus-cruise lifting motor is presented in Fig. 16 with the hover point indicated. The limits of the map are captured within the motor simulation. The key limit is the peak torque limit (153 ft-lb). However, voltage-based limits also limit torque in the high-speed and high-torque region. The no-load speed of the motor was treated as a maximum speed limit for the motor before damage occurs. While existing limits allowed control design metrics to be met, no pilot feedback has been provided to date, so powertrain size may be subject to change.

Figure 16 demonstrates motor operations with flux weakening (FW) and without flux weakening (NFW) control (Ref. 23). FW control is an available inverter technology which weakens the effect of back-electromotive force, allowing motors to operate at higher speeds by using non-zero D-current. It is believed that FW control would be a viable solution to improve the performance of motors sized by NDARC. The benefit of FW control is that it increases available torque at higher motor speeds without increasing the weight of the motor. Assuming the motor operates at the rated motor voltage, the torque load will follow the path of the NFW line in Fig. 16; but with FW, the torque load descent will be more gradual.

The area in Fig. 16 to the left of the NFW line represents the region of typical torque-speed operations of the motor. The extension of peak torque to the right from the base speed of

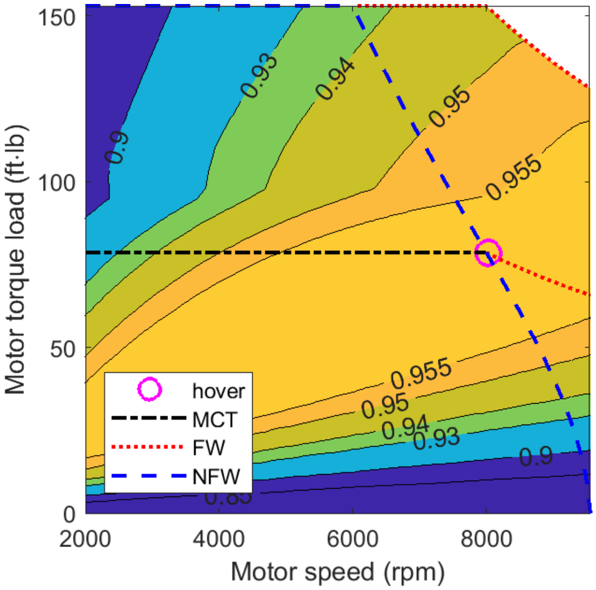

Figure 16. Example lift-plus-cruise lifting motor torque-speed map with lines of constant motor efficiency.

5,999 RPM is achieved by using a battery which is higher voltage than the rated voltage of the motor. It is typical for motor manufacturers to provide a range of voltage operation for a motor.

An example of RTPM predicted motor parameters for the lift-plus-cruise lifting motor were recorded in Table 4. All parameters, except motor inertia, were sized collaboratively using NDARC and the RTPM sizing methodology. The motor inertia of 0.0208 slug-ft^2 was sized based on a motor with similar torque capability in a motor manufacturer's catalog.

Table 4. Lift-Plus-Cruise Lifting Motor Parameters

Parameter	Value
Rated Speed (ω_m^r)	8,000 RPM
Rated Current (I_m^r)	312.9 A$_{pk}$
Rated Torque (τ_m^r)	78.6 ft-lb
Peak Torque (τ_m^p)	153.0 ft-lb
Base Speed (ω_b)	5,999 RPM
No-load Speed (ω_m^{nl})	9,558 RPM
Gear Ratio (GR)	7.616
Motor Inertia	0.0208 slug-ft^2
Rated Efficiency (η_m)	96%
Inverter Efficiency (η_I)	99%

FLIGHT CONTROL LAWS

Control Design Approach

Figure 17 shows a high-level block diagram of the control system analysis model, which consists of an EMF architecture and subsystems for control allocation, electronic speed controllers (ESCs), powertrain, and bare-airframe. For initial control design, a simplified powertrain model, which includes friction and constant motor torque and speed limits, was used. First, the ESCs, which consist of a proportional-integral (PI) architecture, were designed to achieve fast rise times without excessive torque limiting, which is an important design consideration for eVTOL aircraft. These ESCs and simplified motor models were integrated into a higher-level flight control system analysis model in CONDUIT, a flight control design software developed by the U.S. Army Combat Capabilities Development Command Aviation & Missile Center (DEVCOM AvMC). This control system analysis model also included the linear bare-airframe models extracted from FLIGHTLAB, which were verified using the methods described in a previous section. Control system gains were optimized using CONDUIT to meet a comprehensive set of stability, performance, and handling qualities requirements at various flight conditions spanning the flight envelope (Ref. 24).

The optimized control system gains were integrated into the full flight envelope control laws, which included considerations for scheduling trim control positions, control allocation, and gains; transient mode switching; anti-windup integrator logic; conversion from continuous to discrete blocks; and other elements and logic not included in the CONDUIT analysis model. Notably, the lift-plus-cruise simulation models the flight dynamics changes and implements a rotor stop hysteresis in the control logic for transition between rotor-borne and fully wing-borne flight.

Effect of Product of Inertia on Yaw Control Effectiveness

Accurate modeling of the rotor control effectiveness is required for determining control allocation during the control law design process. When examining the lift-plus-cruise configuration's yaw control effectiveness derivatives, several unexpected trends were seen which are due to the nonzero product of inertia I_{xz} of the aircraft configuration, and the resulting coupling of the vehicle rotational response to yaw and roll moments.

The aircraft moment equations of motion are given by:

$$\begin{bmatrix} L \\ M \\ N \end{bmatrix} = \begin{bmatrix} I_{xx} & 0 & -I_{xz} \\ 0 & I_{yy} & 0 \\ -I_{xz} & 0 & I_{zz} \end{bmatrix} \begin{bmatrix} \dot{p} \\ \dot{q} \\ \dot{r} \end{bmatrix} + \begin{bmatrix} p \\ q \\ r \end{bmatrix} \times \begin{bmatrix} I_{xx} & 0 & -I_{xz} \\ 0 & I_{yy} & 0 \\ -I_{xz} & 0 & I_{zz} \end{bmatrix} \begin{bmatrix} p \\ q \\ r \end{bmatrix} \tag{9}$$

When Eq. 9 is linearized and put into state-space form, the lateral/directional stability and control derivatives become coupled through the product of inertia I_{xz}, and are often referred to as the primed derivatives (Ref. 25):

$$L_i' = \frac{L_i + (I_{xz}/I_{xx})N_i}{1-(I_{xz}^2/I_{xx}I_{zz})} \tag{10}$$

$$N_i' = \frac{N_i + (I_{xz}/I_{zz})L_i}{1-(I_{xz}^2/I_{xx}I_{zz})} \tag{11}$$

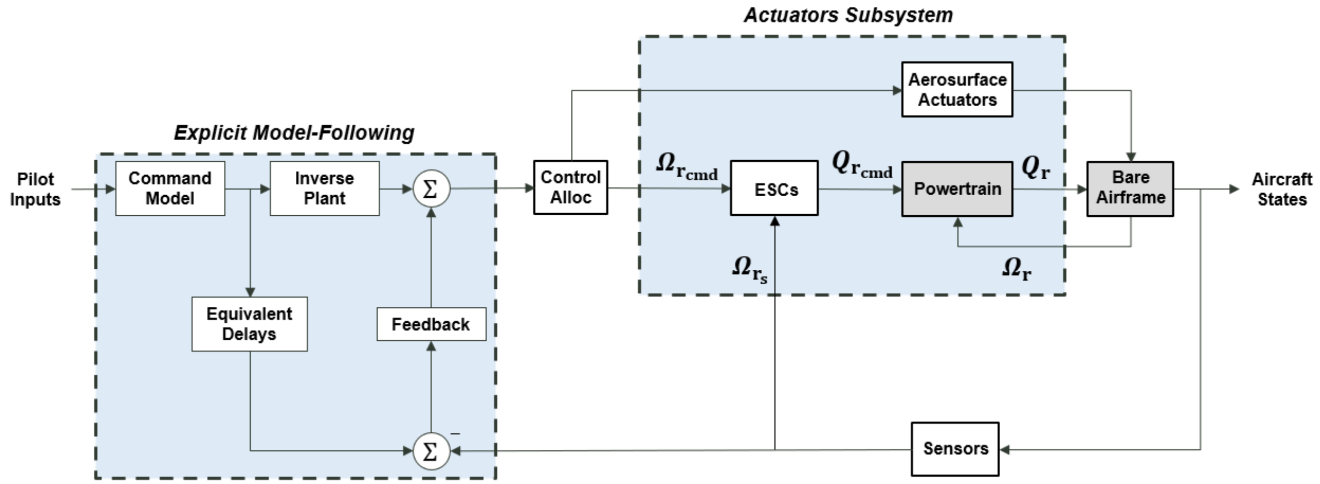

Figure 17. Control system design and analysis model.

Table 5 shows the lift-plus-cruise configuration yaw derivatives for rotor torque N'_{Q_i} and rotor speed N'_{Ω_i}. The yaw derivatives to rotor torque have the expected signs (opposite of the rotor rotational direction) and magnitudes (same magnitudes for the outboard rotors, and slightly smaller magnitudes of the inboard canted rotors). However, examination of the yaw derivatives to rotor speed shows several unexpected trends. First, the forward inboard rotors (which are canted), generate an order of magnitude *less* yaw rate than the forward outboard rotors (which are not canted) ($|N'_{\Omega_{\text{inboard}}}| = 0.00022$ and $|N'_{\Omega_{\text{outboard}}}| = 0.0016$). The second unexpected trend is that the sign of the yaw derivatives to rotor speed for the rear rotors does not correlate with their rotational direction.

When the rolling moment due to a control input L_i is significantly larger than the yawing moment N_i, the rolling moment can start to dominate the primed yaw derivative N'_i (Eq. 11), even when I_{xz} is significantly smaller than I_{zz}, which is the case for the rotor speed derivatives N_Ω and L_Ω for this vehicle.

Figures 18(a) and 18(b) show variations in the primed roll and yaw moment derivatives with increasing product of inertia I_{xz} as a percent of the z-axis moment of inertia I_{zz}. For the rotor speed derivatives (Fig. 18(a)), the roll moment generated is significantly larger than the yaw moment generated for both inboard and outboard rotors, which dominates the primed yaw derivatives. This results in significant changes to the primed yaw derivatives as a function of I_{xz}, even when I_{xz} is only a few percent of I_{zz}. This is most notable for the rear outboard rotors (Rotors 5 and 8), where the primed yaw derivatives N'_{Ω_i} are near zero for small values of I_{xz}/I_{zz}. Increasing values of I_{xz} also result in the uncanted outboard rotors generating more yaw moment than the canted inboard rotors in the front. In contrast, the primed roll derivatives L'_{Ω_i} do not vary significantly as a function of I_{xz}.

The opposite trend can be seen for the rotor torque derivatives (Fig. 18(b)), where the yaw moment is dominant. Here the primed yaw derivatives N'_{Q_i} do not vary significantly as a function of I_{xz}, while the primed roll derivatives L'_{Q_i} do.

For an RPM controlled vehicle, such as the lift-plus-cruise configuration considered here, the effect of the product of inertia I_{xz} on the primed yaw rotor speed derivatives N'_{Ω_i} will impact the control allocation design of the vehicle—whether a yaw moment demand from the control system should command an increase or decrease in a rotor's RPM. The product

Table 5. Lift-Plus-Cruise Yaw Control Derivatives ($I_{xz} = 1351.9$ slug-ft^2)

		Left		Right	
		Outboard	Inboard	Inboard	Outboard
Forward	Number	1	2	3	4
	Direction	CCW	CW	CCW	CW
	N'_Q [rad/s^2/ft-lb]	4.22×10^{-5}	-4.18×10^{-5}	4.18×10^{-5}	-4.22×10^{-5}
	N'_Ω [1/s]	0.0016	−0.00022	0.00022	−0.0016
Aft	Number	5	6	7	8
	Direction	CW	CCW	CW	CCW
	N'_Q [rad/s^2/ft-lb]	-4.22×10^{-5}	4.18×10^{-5}	-4.18×10^{-5}	4.22×10^{-5}
	N'_Ω [1/s]	0.0015	0.0015	−0.0015	−0.0015

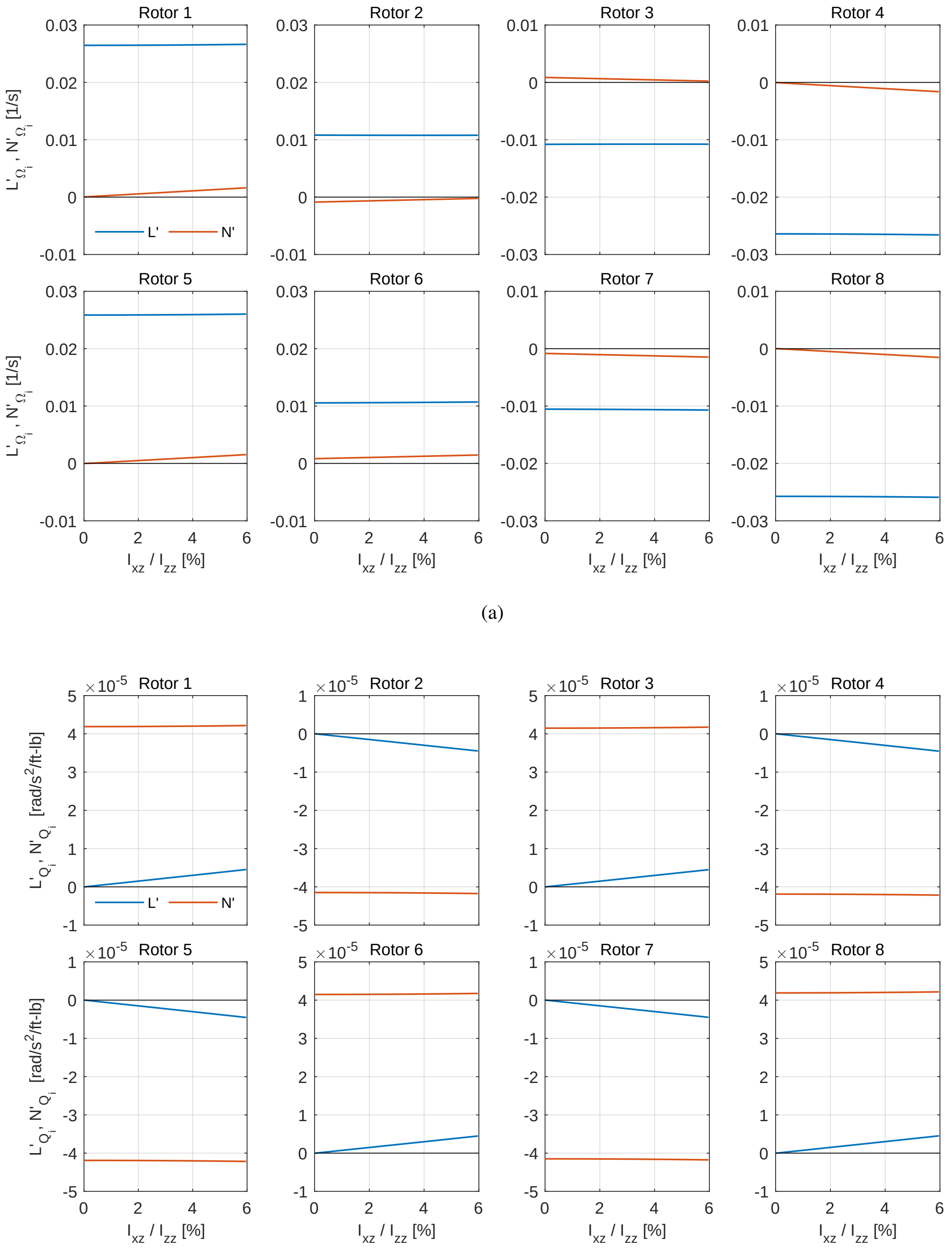

Figure 18. lift-plus-cruise yaw and roll control derivatives to (a) rotor speed and (b) rotor torque inputs as a function of product of inertia I_{xz}.

of inertia I_{xz} is typically hard to estimate, especially in the preliminary design phase, but will impact the control design. Updates to the yaw control allocation should be made as better estimates of I_{xz} become available. In addition, the control system should be assessed for robustness to variations in I_{xz}, since different passenger and payload configurations may result in different values of I_{xz}.

VMS INTEGRATION

Piloted evaluations of the two aircraft models will be performed in the VMS. Figure 19 shows the top-level architecture for integration of systems into the VMS. The three primary components include the (1) FLIGHTLAB flight dynamics model, (2) high-fidelity powertrain, and (3) control laws. The sim host manages the scheduling by calling each component sequentially. First, the host receives control inputs from the sim cab, which are provided to the control laws. A required torque is commanded by the controller and sent to the powertrain. The powertrain then determines actual torque output and sends that information to the FLIGHTLAB model. The airframe model iterates one time step and feeds back the new state information to all other components.

In preparation for the formal simulation evaluation, several steps were taken to ensure a smooth transition to the VMS. The first was to integrate the FLIGHTLAB flight dynamics model, control laws, and powertrain into a single desktop simulation environment. Basic checks, including trims, doublet responses, and frequency sweeps, are to be performed at select conditions to ensure the input/output variables to each component are correct and units are accounted for. The verified combined model can then be integrated into a fixed-base engineering simulator, where the visuals and pilot inceptors are connected to the model to allow for initial checkouts. Once the model has been tested in a real-time environment, it will be sent to the VMS for integration.

CONCLUDING REMARKS

This paper described the model development of two eVTOL configurations to be used in a piloted simulation study investigating the handling and ride qualities of these new types of aircraft for both civilian and military applications. The three primary components (flight dynamics model, powertrain, control laws) were discussed for the lift-plus-cruise configuration as well as their integration into the VMS.

Stability derivatives for the lift-plus-cruise configuration showed no major discontinuities among rotors on and rotors off flight and the trends suggest 40 kt intervals for linear models were sufficient for control law development. The linear models aligned closely with the nonlinear models at the handling qualities frequencies of interest at hover and cruise. One interesting finding was that yaw derivatives to rotor speed exhibited unexpected behavior due to a nonzero product of inertia I_{xz}. This affects control allocation design and control laws should be assessed for robustness to I_{xz} variations.

Integrating with the VMS is being conducted through a buildup approach of desktop integration → fixed-base engineering simulator → VMS to ensure a smooth transition with minimal conflicts.

ACKNOWLEDGMENTS

The authors would like to thank Mr. Matthew Gladfelter with Advanced Rotorcraft Technology, Inc. for his support with the FLIGHTLAB software and model development and analysis. The authors would also like to thank Ms. Melissa May and Mr. Ahmad Alhayek, NASA Ames Aeromechanics Branch interns (summer 2024), for their work on tiltwing system identification and conversion corridor development. This work was funded by the Revolutionary Vertical Lift Technology project.

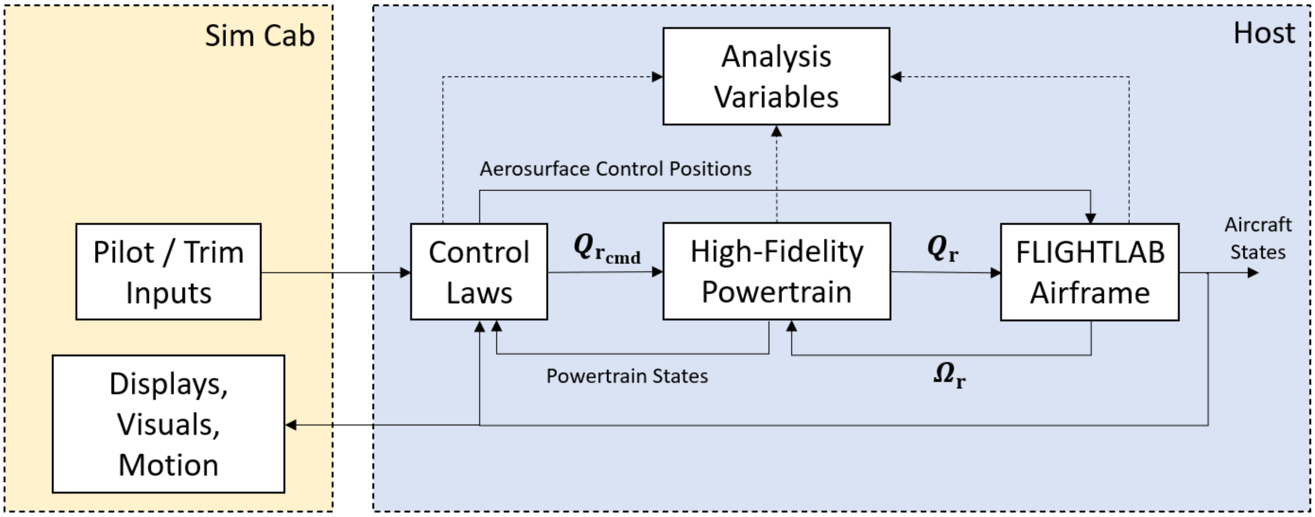

Figure 19. Architecture diagram for systems integration of the control laws, powertrain model, and FLIGHTLAB flight dynamics model into the Vertical Motion Simulator.

REFERENCES

1. Hirschberg, M., “Vertical Flight Society Electric VTOL Directory Hits 1,000 Designs,” April 22, 2024, https://evtol.news/news/press-release-vertical-flight-society-electric-vtol-directory-hits-1000-designs.

2. Air Force Research Laboratory Public Affairs, “AFWERX Agility Prime - A New Era of Aerospace,” November 22, 2021, https://www.afrl.af.mil/News/Article/2850369/afwerx-agility-prime-a-new-era-of-aerospace/.

3. Malpica, C., Withrow-Maser, S., Aires, J., Schuet, S., Suh, P., Barnes, K., Hanson, C., Ruan, A., Altamirano, G., Foster, J., “Handling Qualities of Multirotor RPM-Controlled Electric-Vertical Take-Off and Landing (eVTOL) Aircraft for Urban Air Mobility (UAM),” Vertical Flight Society’s 79th Annual Forum & Technology Display, West Palm Beach, FL, May 16-18, 2023.

4. Withrow-Maser, S., Aires, J., Ruan, A., Malpica, C., Schuet, S. “Evaluation of Heave Disturbance Rejection and Control Response Criteria on the Handling Qualities Evaluation of Urban Air Mobility (UAM) eVTOL Quadrotors Using the Vertical Motion Simulator,” VFS Aeromechanics for Advanced Vertical Flight Technical Meeting, San Jose, CA, Jan 25-27, 2022.

5. Aires, J., Withrow-Maser, S., Ruan, A., Malpica, C., Schuet, S. “Analysis of Handling Qualities and Power Consumption for Urban Air Mobility (UAM) eVTOL Quadrotors with Degraded Heave Disturbance Rejection and Control Response,” Vertical Flight Society’s 78th Annual Forum & Technology Display, Fort Worth, TX, May 10-12, 2022.

6. Altamirano, G. , Matt, J., Foster, J., Suh, P., Hanson, C., Malpica, C., and Schuet, S., “Flying Qualities Analysis and Piloted Simulation Testing of a lift-plus-cruise Vehicle with Propulsion Failures in Hover and Low-Speed Conditions,” Vertical Flight Society’s 79th Annual Forum & Technology Display, West Palm Beach, FL, May 2023.

7. Suh, P., Barnes, K., Trevino, J., Hanlon, P. A., Hunker, K. R., Fernandez, X. C., Sadey, D. J., Valco, M. J., Tallerico, T., Malpica, C., “Real-Time eVTOL Powertrain Modeling for the NASA Vertical Flight Simulator,” Vertical Flight Society’s 81st Annual Forum & Technology Display, Virginia Beach, VA, May 2025.

8. Federal Aviation Administration, “Handling Qualities Test Guide for Powered Lift VTOL Capable Aircraft with Indirect Flight Controls and Operating in Day Time Visual Flight Rules,” DOT/FAA/TC-23/59, March 2024.

9. European Union Aviation Safety Agency, “Special Condition Vertical Take-Off and Landing (VTOL) Capable Aircraft,” SC-VTOL-02, June 2024.

10. European Organisation for Civil Aviation Equipment, “Guidance on VTOL Flight Control Handling Qualities Verification,” ED-295, July 2024.

11. Gladfelter, M., He, C., Saberi, H., Malpica, C., Johnson, W., Silva, C., “Enhanced Flight Dynamics Models with Aerodynamic Interference for Real-Time Simulation of VTOL Concept Vehicles,” Vertical Flight Society’s 79th Annual Forum & Technology Display, West Palm Beach, FL, May 16-18, 2023.

12. Silva, C., Johnson, W., Antcliff, K. R., and Patterson, M. D., “VTOL Urban Air Mobility Concept Vehicles for Technology Development,” AIAA 2018-3847, Aviation Technology, Integration, and Operations Conference, Atlanta, GA, June 25-29, 2018.

13. Whiteside, S. K. S., Pollard, B. P., Antcliff, K. R., Zawodny, N. S., Fei, X., Silva, C., Medina, G. L., “Design of a Tiltwing Concept Vehicle for Urban Air Mobility,” NASA TM-20210017971, June 2021.

14. International Organization for Standardization, “Mechanical vibration and shock - Evaluation of human exposure to whole-body vibration,” ISO 2631-1, July 1997.

15. Gladfelter, M., He, C., Saberi, H., Caudle, D., Singh, R., Malpica, C., Silva, C., “Enhancements, Verification, and VMS Integration of VTOL Concept Vehicle Simulation Models,” Vertical Flight Society’s 80th Annual Forum & Technology Display, Montreal, Quebec, Canada, May 2024.

16. Tischler, M. B., Remple, R. K., *Aircraft and Rotorcraft System Identification,* AIAA Education Series, 2012, pp. 671-675.

17. Berger, T., Lopez, Mark J. S., Wagner, Aaron M., Tischler, Mark B., “Guidelines for System Identification of Multirotor Vehicles with Highly Correlated Inputs,” Vertical Flight Society’s 76th Annual Forum & Technology Display, Virginia Beach, VA, Oct 2020.

18. Nadell, S. J., Berger, T., DiMarco, C., Lopez, M. J. S., “System Identification and Stitched Modeling of the ADAPT™ Winged Compound Helicopter Scaled Demonstrator,” Vertical Flight Society’s 78th Annual Forum & Technology Display, Ft. Worth, TX, May 2022.

19. Malpica, C., Suh, P., and Silva, C., “Flight Dynamics Conceptual Exploration of Multirotor eVTOL,” Vertical Flight Society’s 80th Annual Forum & Technology Display, Montreal, Quebec, Canada, May 2024.

20. Krishnan, R., *Electric Motor Drives: Modeling, Analysis, and Control*, Prentice-Hall, Upper Saddle River, NJ, 2001.

21. Johnson, W., Silva, C., Solis, E., "Concept Vehicles for VTOL Air Taxi Operations," AHS Technical Conference on Aeromechanics Design for Transformative Vertical Flight, San Francisco, CA, January 2018.

22. Johnson, W., "NDARC NASA Design and Analysis of Rotorcraft," NASA/TP-2015-218751, NASA, Moffett Field, CA, 2015.

23. Bolognani, S., Calligaro, S., Petrella R., Pogni, F., "Flux-weakening in IPM motor drives: Comparison of state-of-art algorithms and a novel proposal for controller design," Proceedings of the 2011 14th European Conference on Power Electronics and Applications, Birmingham, UK, 2011.

24. Tischler, M. B., Berger, T., Ivler, C. M., Mansur, M. H., Cheung, K. K., Soong, j. Y., *Practical Methods for Aircraft and Rotorcraft Flight Control Design*, AIAA Education Series, 2017.

25. McRuer, D. T., Graham, D., Ashkenas, I., *Aircraft Dynamics and Automatic Control*, Princeton University Press, 2014.